

Predictive Risk Analytics for Weather-Resilient Operation of Electric Power Systems

Payman Dehghanian , *Member, IEEE*, Bei Zhang, *Member, IEEE*, Tatjana Dokic , *Student Member, IEEE*, and Mladen Kezunovic, *Life Fellow, IEEE*

Abstract—Day-to-day operation of the electricity grid generation, transmission, and distribution is environmentally driven and closely dependent on evolving weather patterns. This paper introduces several new weather-driven analytics for accurate spatial-temporal electricity generation forecasts, asset health and reliability assessment, probabilistic load forecasts, and electricity market simulations. A new risk metric is suggested, which accounts for the weather hazards, grid vulnerability, and financial consequences in the face of changing weather patterns and associated meteorological predictions over time. New mitigation formulations for power system topology control through transmission line switching for fast and timely recovery of the weather-caused electricity outages are suggested. The proposed decision support tool enables the operators to predictively evaluate the high-risk weather threats and consequently plan on how to safeguard the grid when exposed to forecasted weather-driven incidents. The efficiency of the proposed toolset is illustrated by application to a part of the IEEE 73-Bus test system.

Index Terms—Weather, forecast, risk, decision making, topology control, vulnerability, mitigation.

I. INTRODUCTION

THE Electricity grid is vulnerable to various threats: outdated flexibility of the system, aged assets, volatile weather patterns, and cyber-physical security threats. With the rapid deployment of intermittent renewable generation, growing demand to ensure a higher quality electricity to end customers, and intensified public focus and regulatory oversights, there is an urgent need to enrich the power delivery infrastructure resilience as well as to reduce and mitigate such threatening risks [1]–[3].

It has been clear over the past couple of years that further considerations beyond the classical *reliability-oriented* view are required for keeping the lights on at all times. This is evidenced by an increase in catastrophic weather-caused grid outages, such

Manuscript received August 1, 2017; revised December 13, 2017; accepted March 15, 2018. Date of publication April 12, 2018; date of current version December 14, 2018. Paper no. TSTE-01026-2016. (*Corresponding author: Payman Dehghanian.*)

P. Dehghanian is with the Department of Electrical and Computer Engineering, George Washington University, Washington, DC 20052 USA (e-mail: payman@gwu.edu).

B. Zhang is with GE Energy Consulting, Schenectady, NY 12345 USA (e-mail: bei.zhang@ge.com).

T. Dokic and M. Kezunovic are with the Department of Electrical and Computer Engineering, Texas A&M University, College Station, TX 77843 USA (e-mail: Tatjana.djokic@tamu.edu; kezunov@ece.tamu.edu).

Color versions of one or more of the figures in this paper are available online at <http://ieeexplore.ieee.org>.

Digital Object Identifier 10.1109/TSTE.2018.2825780

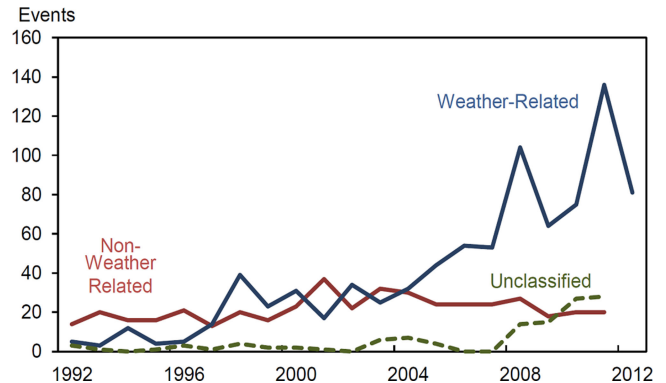


Fig. 1. Weather-dependent outages in the US within 1992–2012 [2].

as thunderstorms, hurricanes, heavy rain, etc. as shown in Fig. 1. As the leading cause of power outages in the United States, a total of 178 weather disasters occurred from 1980's to 2014 in the US alone, 8 of which occurred in 2014, with the overall damages exceeding the US \$1 trillion [1]–[5]. Various industries were halted for hours, if not days, and dozens of people in need of special health care lost their lives due to sustained loss of electricity and inability to swiftly restore the power [3]–[6].

Numerous researchers have studied the impact of environmental factors and weather variations on various aspects of power system operation, studying: different techniques for weather-driven wind and solar generation forecasts in [7]–[10]; robust models for electricity market simulations considering weather uncertainties in [11]–[13], and electricity market decision making risks and operational concerns in [14]–[16]; impact of weather variations and weather-caused overloading conditions on reliability of the electric assets over time in [17]–[19]; advanced models for weather-driven load forecasts in [20]–[22]; technologies on early warning systems for prediction of disastrous weather outages in [23]–[25]; and resiliency assessment of the grid in the face of severe climate change and adverse weather conditions in [26]–[28], among others.

Different from the previous studies, our paper addresses (a) a weather-driven technique based on spatial-temporal correlations for both non-renewable and renewable generation as well as demand forecasts, (b) a Neural Network framework for weather-driven assessment of the asset health and reliability over time, (c) a weather-driven framework and probabilistic modeling for the wholesale electricity market simulations to account for the grid vulnerabilities in exposure to continuous weather changes,

(d) a new risk metric and predictive risk map to be presented to operators at every hour aiming at improving preparedness in response to weather-driven risks and environmental threats, and (e) a corrective optimization toolset suggesting risk-based mitigation strategies based on the network topology control through transmission line switching to alleviate the critical weather-driven risks across the grid.

The remainder of the paper is structured as follows. The proposed analytics, revealing the system and equipment susceptibility to weather changes in generation, transmission, and distribution levels of power systems, are introduced in detail in Section II. Section III is devoted to a new risk-based analytical framework to quantify the system operation risk in exposure to weather threats. Section IV suggests a mitigation decision optimization in the face of extreme weather conditions. Numerical case studies are conducted in Section V followed by conclusions in Section VI.

II. WEATHER-DRIVEN ANALYTICAL FRAMEWORKS IN ELECTRIC POWER SYSTEMS

A. Electricity Generation: Weather Impacts Modeling

Forecasts of the electricity generated through variable renewables such as wind and solar are closely driven by measured and modeled historical and real-time meteorological and environmental factors. Numerous techniques and prediction models have been proposed in the literature on accurate forecast of wind power in different time scales: immediate-short-term (8-hour-ahead), short-term (day-ahead), and long-term (multiple days-ahead) [10], [29]. In Most of the proposed wind prediction techniques for cost-effective grid operations, environmental dynamics of temperature is utilized. Various weather-data driven techniques for prediction of solar generation are proposed and extensively studied in the literature [7]–[9], [30]. While most of the suggested forecasting techniques have been driven solely based on the local meteorological measurements, the spatial correlations of solar sites are also considered in a few studies [7], [10]. Such studies revealed that the forecast accuracy could be significantly improved when spatial correlations are considered.

The conventional sources of electricity generation are also directly or indirectly affected by the continuous weather variations. Temperature, pressure, precipitation, etc. are among the influential factors on the supply of hydroelectric production through a shift in the inflow of water. The *capacity* and *efficiency* of thermal coal-fired generating units are also affected by the cooling water temperature. Besides, the temperature influences the generation efficiency due to the Carnot's theorem [16].

1) *Modeling Weather Impacts on Coal-Fired Thermal Power Generation:* A new data-driven statistical technique to manage the weather-driven prediction of generation *capacity* and *efficiency* for system coal-fired thermal generating units is proposed. The proposed training process aims to provide the conditional probability distribution $P(y|\mathbf{X})$ of a certain parameter, where y is the focused output to be predicted and can be *capacity* and/or *efficiency* of the thermal units and $\mathbf{X} = [x_1, x_2, \dots, x_n]$ can be the possible factors that may affect the output y . Here,

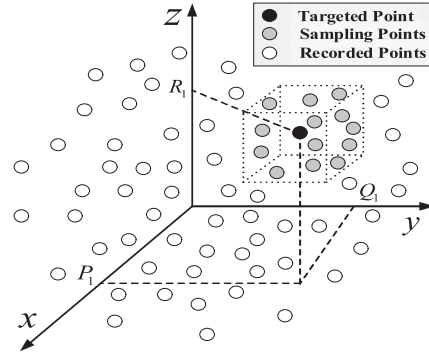


Fig. 2. Illustration of the sampling process for weather-driven capacity and efficiency prediction of thermal generating units as well as the electrical load.

the \mathbf{X} vector contains a set of weather inputs acquired from weather forecasts, e.g., water discharge, temperature, humidity, precipitation, wind speed, and gauge height. Statistical methods are adopted and samples are taken to estimate the output probability distributions. Not only are the outputs corresponding to the exact input \mathbf{X} , but also those within a range of $\mathbf{X} \pm \Delta x$ are sampled. Such considerations are taken into account as (1) errors exist in the weather inputs and it is, therefore, inaccurate to sample solely the outputs with the exact input \mathbf{X} ; (2) exact input \mathbf{X} may not exist in the historical dataset, and thus, the data around a particular point are employed to approximate the corresponding output.

The sampling process is briefly illustrated in Fig. 2. If the goal is to predict the probability distribution of the output with a set of measured (or recorded) inputs (P_1, Q_1, R_1) , the historical data for which the inputs are within the range of $[P_1 - \sigma_1 \times P_1, P_1 + \sigma_1 \times P_1]$, $[Q_1 - \sigma_2 \times Q_1, Q_1 + \sigma_2 \times Q_1]$, $[R_1 - \sigma_3 \times R_1, R_1 + \sigma_3 \times R_1]$ where σ_1, σ_2 and σ_3 are relatively small values are sampled. In the case of higher number of inputs, the cube will turn into a hypercube. Note that the bigger the σ is, the larger the sampling space will be, leading to a more accurate forecast with the expense of higher computational burden. When there is enough historical data available, even a small value of σ will result in many sample points. In such circumstances, selection of σ should be carefully done. In order to efficiently compromise the computational burden and output accuracy, we ensured here that at least 100 samples exist within each selected cube in Fig. 2.

The sampled data are utilized to assess the probability distribution using certain distribution fitting techniques. In this study, the outputs are assumed to follow the normal probability distributions. While the approach is generic enough to accommodate any other variation of the normal distribution (such as a wider-tailed family of distributions with greater robustness as an alternative to the normal distributions [31]) as well as other non-Gaussian family of distributions (e.g., Weibull, etc.) [32]–[34], this assumption is supported by multiple reasons: (a) it is easy to work with mathematically and computationally (e.g., the summation of normal distributions is still a normal one, and the marginal distribution of multivariate normal distribution is also a normal); (b) in many practical cases, the methods developed using such theory works quite well even when the distribu-

tion is not normal. According to Central Limit Theorem (CLT), with the increase in the sample size (sufficiently large), the distribution of the random variables approaches the normal distribution irrespective of the shape of the original distribution [35]. Due to the fact that the sample size of the considered random variables are large enough, normal distribution can be reasonably adopted; (c) the normal distribution maximizes information entropy, i.e., the measure of the uncertainty associated with a random variable, among all distributions with known mean and variance [35].

Employing the method of moments, the normal distribution parameters are approximated through samples' mean μ' and standard deviation σ' . The approximate probability distribution can be then obtained denoted as $P'(y|\mathbf{X}) \sim N(\mu', \sigma')$. The mean value μ' of a sample can be adopted to predict the single output value corresponding to a certain input \mathbf{X} . Therefore, the sensitivity relationship between the output and certain input x_i can be easily characterized by having other input variables fixed and running the single value prediction while changing the value of x_i in a certain range. The slope of the resulting graph denotes the sensitivity of the output to the certain input x_i of interest. Rather than predicating a single-value output, it would be very helpful to provide information on how vulnerable a generating *capacity* or *efficiency* is under certain weather conditions \mathbf{X} . Suppose an output and input relationship is expressed by $y = R(\mathbf{X})$. The sensitivity index corresponding to a certain input vector $\mathbf{Z} = [z_1, z_2, \dots, z_n]$ can be defined as the total differential of $R(\mathbf{X})$ at the point \mathbf{Z} , as defined in (1.a).

$$dy = \frac{\partial y}{\partial x_1} \Big|_{\mathbf{x}=\mathbf{z}} \cdot \Delta x_1 + \frac{\partial y}{\partial x_2} \Big|_{\mathbf{x}=\mathbf{z}} \cdot \Delta x_2 + \dots + \frac{\partial y}{\partial x_n} \Big|_{\mathbf{x}=\mathbf{z}} \cdot \Delta x_n \quad (1.a)$$

Since the exact relation $R(\mathbf{X})$ may not be clearly known in many cases, numerical techniques, such as the one in (1.b), is employed to approximate the total differential in (1.a).

$$dy \approx (\mu'_{\mathbf{x}=[z_1+\Delta z_1, z_2, \dots, z_n]} - \mu'_{\mathbf{x}=[z_1-\Delta z_1, z_2, \dots, z_n]}) + (\mu'_{\mathbf{x}=[z_1, z_2+\Delta z_2, \dots, z_n]} - \mu'_{\mathbf{x}=[z_1, z_2-\Delta z_2, \dots, z_n]}) + \dots + (\mu'_{\mathbf{x}=[z_1, z_2, \dots, z_n+\Delta z_n]} - \mu'_{\mathbf{x}=[z_1, z_2, \dots, z_n-\Delta z_n]}) \quad (1.b)$$

where, $\mu'_{\mathbf{x}=[z_1+\Delta z_1, z_2, \dots, z_n]}$ denotes the mean value of the samples around the input vector \mathbf{Z} .

2) *Modeling Weather Impacts on Solar Power Generation Forecast*: A probabilistic graphical data-driven model, the Gaussian Conditional Random Field (GCRF), is suggested to predict the solar generation output. The model is generic to be applied, with minor adjustments, to forecast of other types of renewables (e.g., wind). The proposed technique can well exploit the correlations among output variables, resulting in significant improvements in the prediction accuracy. Besides, its Gaussian characteristics furnish the inference and improve the learning efficiency [36]. The GCRF model provides a probabilistic framework for exploiting complex dependence structure among output variables, which can help model both the spa-

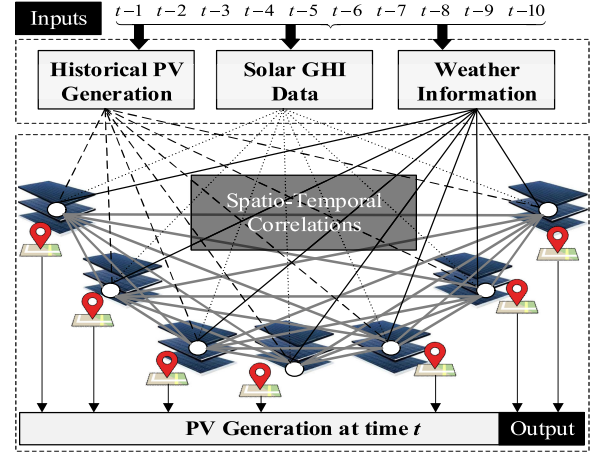


Fig. 3. Spatio-temporal correlations in the proposed GCRF model.

tial and temporal correlations among different solar generation stations (see Fig. 3). The primary goal of this model is to discover the conditional distribution $P(\mathbf{Y}|\mathbf{X})$ through a large volume of historical data, with which the output variables can be efficiently predicted. $\mathbf{Y} = [y_1^t, y_2^t, \dots, y_N^t]^T$ is the forecasted solar output in multiple stations (1 to N) at the next time interval t ; \mathbf{X} represents the historical solar measurements in different stations, as (2):

$$\mathbf{X} = [x_1^{t-1}, x_1^{t-2}, \dots, x_1^{t-m_1}, x_2^{t-1}, x_2^{t-2}, \dots, x_2^{t-m_2}, \dots, x_N^{t-1}, x_N^{t-2}, \dots, x_N^{t-m_N}] \quad (2)$$

The conditional distribution $P(\mathbf{Y}|\mathbf{X})$ is expressed in (3):

$$P(\mathbf{Y}|\mathbf{X}) = \frac{1}{Z(\mathbf{X}, \alpha, \beta)} \exp \times \left(\sum_{i=1}^N \Phi(\alpha, y_i, \mathbf{X}) + \sum_{j \neq i} \Psi(\beta, y_i, y_j, \mathbf{X}) \right) \quad (3)$$

where $\Phi(\alpha, y_i, \mathbf{X})$ is called the association potential that links the output variable y_i to the input vector \mathbf{X} ; $\Psi(\beta, y_i, y_j, \mathbf{X})$ is the interaction potential that correlates the two output variables y_i and y_j [37]; The Φ and Ψ are approximated by linear combinations of pre-determined feature functions with corresponding parameters α and β , as denoted in (4.a) and (4.b).

$$\Phi(\alpha, y_i, \mathbf{X}) = \sum_{k \in K} \alpha_k f_k(y_i, \mathbf{X}) \quad (4.a)$$

$$\Psi(\beta, y_i, y_j, \mathbf{X}) = \sum_{l \in L} \beta_l g_l(y_i, y_j, \mathbf{X}) \quad (4.b)$$

α and β are the parameters to be determined through training of the historical data. If the feature functions f_k and g_l are defined in quadratic forms, as shown in (5) and (6), the association potential Φ and interaction potential Ψ would also be quadratic functions of \mathbf{Y} .

$$f_k(y_i, \mathbf{X}) = -(y_i - R_k(\mathbf{X}))^2, \quad k = 1, \dots, K \quad (5)$$

$$g_l(y_i, y_j, \mathbf{X}) = -e_{ij}^{(l)} S_{ij}^{(l)}(\mathbf{X}) (y_i - y_j)^2 \quad (6.a)$$

$$e_{ij}^{(l)} = \begin{cases} 1 & (i, j) \in G_l \\ 0 & \text{otherwise} \end{cases} \quad (6.b)$$

where, G_l is the graph which imposes the relation between the output variables y_i and y_j . $S_{ij}^{(l)}(\mathbf{X})$ is the function representing similarity between outputs y_i and y_j . And $R_k(\mathbf{X})$ is a single prediction of y_i based on the input variables \mathbf{X} . Under this scenario, the conditional probability distribution $P(\mathbf{Y}|\mathbf{X})$ turns into a multivariate Gaussian distribution $P(\mathbf{Y}|\mathbf{X}) \sim N(\boldsymbol{\mu}, \boldsymbol{\gamma})$, where $\boldsymbol{\mu}$ is the mean vector and $\boldsymbol{\gamma}$ is the covariance matrix. The $P(\mathbf{Y}|\mathbf{X})$ can be eventually rewritten in (7.a) and (7.b).

$$P(\mathbf{Y}|\mathbf{X}) = \frac{1}{Z(\mathbf{X}, \boldsymbol{\alpha}, \boldsymbol{\beta})} \times \exp \left(-\sum_{i=1}^N \sum_{k=1}^{K_i} \alpha_k (y_i - R_k(\mathbf{X}))^2 - \sum_{i,j} \sum_{l \in L} \beta_l e_{ij}^{(l)}(\mathbf{X}) (y_i - y_j)^2 \right) \quad (7.a)$$

$$P(\mathbf{Y}|\mathbf{X}) = \frac{1}{(2\pi)^{N/2} |\boldsymbol{\gamma}|^{1/2}} \times \exp \left(-\frac{1}{2} (\mathbf{Y} - \boldsymbol{\mu})^T \boldsymbol{\gamma}^{-1} (\mathbf{Y} - \boldsymbol{\mu}) \right) \quad (7.b)$$

where, $\boldsymbol{\gamma}^{-1} = 2(\mathbf{Q}_1 + \mathbf{Q}_2)$ and $\mathbf{Q}_1, \mathbf{Q}_2$ are expressed in (8.a), (8.b).

$$Q_{1ij} = \begin{cases} \sum_{k \in K_i} \alpha_k & i = j \\ 0 & i \neq j \end{cases} \quad (8.a)$$

$$Q_{2ij} = \begin{cases} \sum_k \sum_{l \in L_i} \beta_l e_{ik}^{(l)} S_{ik}^{(l)}(\mathbf{X}) & i = j \\ -\sum_{l \in L_i} \beta_l e_{ij}^{(l)} S_{ij}^{(l)}(\mathbf{X}) & i \neq j \end{cases} \quad (8.b)$$

and $\boldsymbol{\mu} = \boldsymbol{\gamma} \cdot \mathbf{b}$ in (7.b), and \mathbf{b} can be calculated in (9).

$$b_i = 2 \left(\sum_{k \in K} \alpha_k R_k(\mathbf{X}) \right) \quad (9)$$

To obtain the conditional probability distributions, the parameters α_k and β_l need to be determined since $f_k(y_i, \mathbf{X})$ and $g_l(y_i, y_j, \mathbf{X})$ are both pre-determined. Such parameters can be learnt through maximizing the conditional log-likelihood of the training sets, as denoted in (10.a) and (10.b), which can be achieved by the application of the gradient descent algorithm.

$$L(\boldsymbol{\alpha}, \boldsymbol{\beta}) = \sum \log P(\mathbf{Y}|\mathbf{X}) \quad (10.a)$$

$$\left(\hat{\boldsymbol{\alpha}}, \hat{\boldsymbol{\beta}} \right) = \arg \max_{\boldsymbol{\alpha}, \boldsymbol{\beta}} (L(\boldsymbol{\alpha}, \boldsymbol{\beta})) \quad (10.b)$$

In our application, the temporal correlations are characterized by the autoregressive model, as described in (11); and the spatial features are correlated to the distance among different solar

stations, as shown in (12).

$$\Phi(\boldsymbol{\alpha}, y_i, \mathbf{X}) = -\alpha_i \left[y_i - \left(c_i + \sum_{m=1}^{p_i} \varphi_{i,m} y_i^{t-m} \right) \right]^2 \quad (11)$$

$$\Psi(\boldsymbol{\beta}, y_i, y_j, \mathbf{X}) = -\beta_{ij} \left[\frac{1}{D_{ij}^2} (y_i - y_j)^2 \right] \quad (12)$$

where, p_i is chosen to be 10 taking into account the previous 10 historical measurements; and $\varphi_{i,m}$ is the coefficient for the Autoregressive (AR) model; D_{ij} is the physical distance between solar stations i and j . Detailed information on the model, training and inference process can be found in [36]. Since the model is of Gaussian nature, $\boldsymbol{\mu}$ can be assessed and employed as the forecasted output value. Moreover, according to multivariate Gaussian distribution characteristic, i.e., its marginal distribution over a subset of random variables is also a Gaussian distribution, the probability distribution of y_i can be obtained in (13):

$$P(y_i|\mathbf{X}) \sim N(\mu_i, \gamma_{ii}) \quad (13)$$

B. Weather-Driven Model for Electricity Demand Forecast

The electricity demand is also dependent on the time of the day, season, and other weather factors as the electricity consumers' behavior is mostly driven by ambient temperature followed by dew point temperature, clouds, precipitation, and winds. There have been numerous studies on the impact of weather on the electric load behavior and load forecast analysis [20]–[22]. In this paper, the data-driven technique proposed earlier [see Fig. 2] is utilized for load forecasts. Accordingly, the weather factors considered in this paper for accurate load forecast are the heating degree days (HDD), cooling degree days (CDD), temperature, dew point, and wind speed as well as the corresponding load measures over time. Both the probability distribution of the demand at time t , and the sensitivity of the output to the corresponding input variables can be assessed.

C. Weather-Driven Asset Health and Reliability Modeling

Most of the grid infrastructures have been designed and operated since long ago and there is large population of equipment (e.g., transformers, circuit breakers, overhead lines, etc.) with the age of over 25–40 years in service today. Assessing the influence of continuous exposure of the grid assets to weather variations over time is a challenge. Some are located and operated under normal climate conditions and some are exposed to especial weather conditions (e.g., dust, sand, salt deposits, humidity, frequent storms, etc.). Sudden changes in temperature and other prevailing weather conditions would also affect the equipment stress and loading, revealing a higher risk to the safe and reliable operation of the grid. As a result, predictive indicators on the weather-driven performance and reliability of equipment would be desirable.

1) *Modeling Weather Impacts on Health Measures of Transformers*: The purpose of transformer condition assessment is to detect and quantify its long-term degradation and remaining

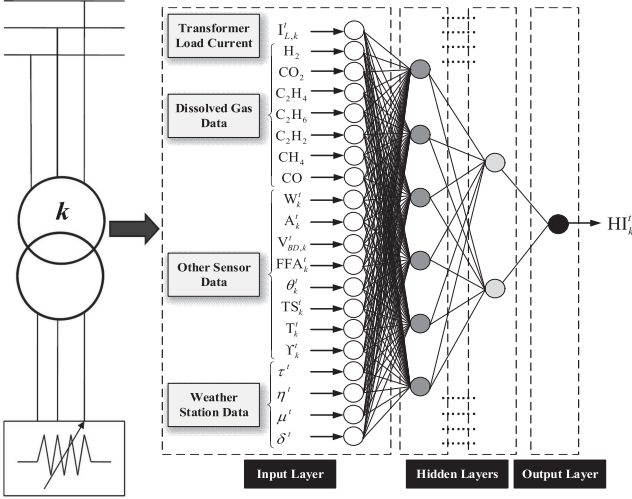


Fig. 4. FFANN framework proposed for transformer health assessment.

life-time. In order to investigate how the reliability and health performance of transformers can be influenced by continuous exposure to weather factors, online asset monitoring data from both electrical and oil testing sensors/monitors as applicable, historical data on transformer loadings, as well as the aging data and corresponding weather information are utilized within a proposed artificial neural network (ANN) mechanism. The developed feed-forward ANN (FFANN) can quantify the health condition of transformers over time as illustrated in Fig. 4. As it can be seen in Fig. 4, the proposed FFANN is composed of many computing elements, called neurons, all working in parallel and are connected by weights. Such weights, adapted via a learning process, encode the knowledge of the network. An input unit represents raw information that is fed into the network and connected to an output layer through one or more layers, called hidden layers [38], [39]. It is commonly known that the number of hidden layers may be selected through trial and error to enhance the predication accuracy. The input layer of the proposed framework consists of 20 neurons, where, $I_{L,k}^t$ is the load current, W_k^t is the paper water content, A_k^t is the acidity level, $V_{BD,k}^t$ is the break down voltage, FFA_k^t is the Furan content in insulating oil, θ_k^t is the loss angle factor, TS_k^t is the total solids in insulating oil, T_k^t is the top oil temperature, γ_k^t is the age, τ^t is the ambient temperature, η^t is the atmospheric pressure, μ^t is the humidity level, and δ^t is the dust level factor of transformer k at time t . The output layer consists of one neuron, ranging between $[0, 1]$ and representing the health index for the transformer: 1 denoting a brand new transformer and 0 associated with one in a poor reliability condition. The health index is a dynamic reliability measure and can be updated over time as new data arrives.

2) *Modeling Weather Impacts on Transmission Lines:* The electrical towers and insulating systems are more likely to fail over time than the overhead lines themselves [40]. Wooden poles begin to rot in 40 years of continuous service, and steel towers would corrode, mostly driven by the weather and environmental drivers. The severe temperature rise/fall is directly governing

the loading of the transmission lines, resulting in an extra heat of the conductors. Such incidents may lead to an unpredicted sag condition of the transmission line, which in some cases, could come in contact with the surrounding environment such as trees and other facilities, resulting in a fault and risk to electric safety. In this study, an online health index for transmission lines is employed, obtained quantitatively through a combination of the condition monitoring data for some line assemblies (e.g., insulators, conductors, etc.) and the inspection data and human judgment for some other elements (e.g., foundations, tower structures, auxiliaries, etc.) [18], [40].

The impact of weather is not solely limited to the mal-operation or failure of the line assemblies. For instance, temperature variations would result in different resistance values of overhead transmission lines which can significantly affect the maximum power capacity, available transfer capability of the line, accuracy of power flows, state estimation, and other power system applications. Additionally, the impact of short-term weather variations (and for example wind speed) on the ampere capacity of transmission lines and the dynamic line rating can also be investigated and integrated into the proposed risk analytics [41]–[44]. In this study, different resistance values for a transmission line in different operation hours are assumed since the line resistance is a direct function of predicted temperature as demonstrated in (14) [40]:

$$R_{T_1} = R_{T_0} [1 + \alpha (T_1 - T_0)] \quad (14)$$

where, $\alpha = 0.0039 [C]^{-1}$ is the temperature coefficient for the aluminum, and R_{T_1} and R_{T_0} are the line resistance values in temperature T_1 and T_0 , respectively.

D. Weather-Driven Model for Electricity Market Simulations

With environmentally-driven generation pattern and load profile at each hour, the electricity market performance would also be affected by weather variations. The results of the introduced models for the impact assessment of weather factors on the loads, generations, and transmission assets are fed into an electricity market simulation framework (the generation and load forecasts are inserted in the form of probability distributions) to realize how such weather considerations would affect the wholesale electricity market performance. The unit commitment model is utilized to optimally dispatch the generating units in a given operation time frame. The model is formulated in (15) with various system and security constraints in (16),

$$\min f = \sum_{i \in G} \sum_{t=t_0}^T (C_{Gi} p_{Gi}^t + C_{RSi} p_{RSi}^t + C_{Ui} s_{Ui}^t + C_{Di} s_{Di}^t) \quad (15)$$

$$\sum_{i \in G} p_{Gi}^t = P_L^t, \quad t = 1, 2, \dots, T \quad (16.a)$$

$$\sum_{i \in G} p_{RSi}^t \geq D_{RS}^t, \quad t = 1, 2, \dots, T \quad (16.b)$$

$$P_{Gi}^t + P_{RSi}^t \leq x_{Gi}^t P_{Gi}^{\max}, \quad i \in G, t = 1, 2, \dots, T \quad (16.c)$$

$$x_{Gi}^t P_{Gi}^{\min} \leq P_{Gi}^t \leq x_{Gi}^t P_{Gi}^{\max}, \quad i \in G, t = 1, 2, \dots, T \quad (16.d)$$

$$0 \leq P_{RSi}^t \leq P_{Gi}^{\max}, \quad i \in G, t = 1, 2, \dots, T \quad (16.e)$$

$$x_{Gi}^t - x_{Gi}^{t-1} \leq s_{Ui}^t, \quad i \in G, t = 1, 2, \dots, T \quad (16.f)$$

$$x_{Gi}^{t-1} - x_{Gi}^t \leq s_{Di}^t, \quad i \in G, t = 1, 2, \dots, T \quad (16.g)$$

$$x_{Gi}^t, s_{Ui}^t, s_{Di}^t \in \{0, 1\}, \quad i \in G, t = 1, 2, \dots, T \quad (16.h)$$

$$P_{Gi}^t - P_{Gi}^{t-1} \leq R_i \Delta t, \quad i \in G, t = 1, 2, \dots, T \quad (16.i)$$

$$P_{Gi}^{t-1} - P_{Gi}^t \leq R_i \Delta t, \quad i \in G, t = 1, 2, \dots, T \quad (16.j)$$

$$-\mathbf{F} \leq \mathbf{H} \cdot \mathbf{P}_G^t \leq \mathbf{F}, \quad t = 1, 2, \dots, T \quad (16.k)$$

where C_{Gi} and C_{RSi} are, respectively, the generation and reserve costs for generating unit i ; P_{Gi}^t and P_{RSi}^t are, respectively, the output power of generator i at time t in energy and reserve markets; C_{Ui} and C_{Di} are, respectively, the start-up and shut-down costs of generator i ; s_{Ui}^t and s_{Di}^t are the start-up and shut-down status variables of generator i at time t ; \mathbf{H} is the distribution factor matrix; and \mathbf{F} is the vector of the transmission line flow limits. Equation (16.a) reflects the energy balance in which P_L^t is the net load demand at time t ; reserve requirement is presented in (16.b) in which D_{RS}^t is the reserve demand at time t . The generation limits of generating units are enforced in (16.c)–(16.e), and x_{Gi}^t indicates their on/off states at time t . Meanwhile, the on/off states of generating units have to meet the constraints in (16.f)–(16.h) and ramping constraints are enforced in (16.i) and (16.j), where R_i is the ramp rate of generating unit i . Transmission line constraints are expressed in (16.k).

As the inputs to the suggested electricity market model are in the forms of probability distributions (of demand and generation), the Point Estimate Method (PEM) is adopted to approximate the probability distribution of the market outputs (e.g., price, system cost, etc.). Different from the Monte Carlo simulations, which randomly selects the input data and need a huge number of simulation records, the PEM method systematically selects some particular input data to simulate the final output. Therefore, the computation burden drastically decreases. Suppose the relationship between the electricity market inputs and outputs is expressed as in (17).

$$\mathbf{F} = \mathbf{g}(\mathbf{Y}) \quad (17)$$

For each input to the electricity market model, suppose a normal probability distribution is assigned and its mean and standard deviation are expressed as μ' and δ' , respectively. Using the 2-PEM technique, two points are selected for each random input variable using (18.a)–(18.c), where m is the total number of random input variables.

$$y_{i,k} = \mu'_i + \zeta_{i,k} \cdot \delta'_i, \quad k = 1, 2 \quad (18.a)$$

$$\zeta_{i,k} = \frac{\lambda_{i,3}}{2} + (-1)^{3-k} \sqrt{m + \left(\frac{\lambda_{i,3}}{2}\right)^2}, \quad k = 1, 2 \quad (18.b)$$

$$\lambda_{i,3} = \frac{E[(y_i - \mu'_i)^3]}{\delta_i'^3} \quad (18.c)$$

The mean value of the output parameter j can be calculated through (19.a)–(19.c).

$$E(F_j) \approx \sum_{i=1}^m \sum_{k=1}^2 w_{i,k} \cdot g_j(\mu'_1, \mu'_2, \dots, \mu'_i, \dots, \mu'_m) \quad (19.a)$$

$$w_{i,k} = \frac{1}{m} (-1)^k \frac{\zeta_{i,3-k}}{\theta_i} \quad (19.b)$$

$$\theta_i = 2\sqrt{m + \left(\frac{\lambda_{i,3}}{2}\right)^2} \quad (19.c)$$

Accordingly, the standard deviation of the output parameter j can be obtained using (20.a) and (20.b).

$$E(F_j^2) \approx \sum_{i=1}^m \sum_{k=1}^2 w_{i,k} \cdot [g_j(\mu'_1, \mu'_2, \dots, \mu'_i, \dots, \mu'_m)]^2 \quad (20.a)$$

$$\delta_{F_j} = \sqrt{E(F_j^2) - [E(F_j)]^2} \quad (20.b)$$

When considering the impacts of weather factors on transmission lines and transformers, not only may the temperature-sensitive characteristics of such equipment change, but also they might not be available at all times due to the weather-driven system operational constraints. Therefore, the topology of the system may change accordingly, and an islanding condition may occur. In such circumstances, the Unit Commitment (UC) model will be conducted in each island separately to ensure the generation and load balance.

III. WEATHER-DRIVEN RISK METRIC FOR POWER SYSTEM

The risk assessment framework is proposed as follows:

$$R_{sys}^t = \sum_{k \in K} \left(P_k^t[T] \cdot \sum_{q \in Q} (P_k^t[E_q|T] \cdot C_k^t(E_q)) \right) \quad (21)$$

where R_{sys}^t is the *State of Risk* for the system (or equipment) at time t ; $P_k^t[T]$ is the *Hazard*, i.e., the probability of an extreme weather condition k with the threat intensity T at time t ; $P_k^t[E_q|T]$ is the *Vulnerability*, i.e., the probability of an abnormal condition E_q in system (or component) performance in the face of the hazardous condition; and $C_k^t(E_q)$ is the *Worth of Loss*, i.e., an estimate of the consequential financial losses. The proposed risk measure is defined as a stochastic process referenced in time and space:

$$R_{sys}^t(x, t) = \sum_{k \in K} \left(P_k^t[T(x, t)] \cdot \sum_{q \in Q} (P_k^t[E_q(x, t)|T(x, t)] \cdot C_k^t(E_q(x, t))) \right) \quad (22)$$

where, x represents the spatial parameter (longitude and latitude) and t reflects the temporal parameter obtained via GPS.

The *hazard* in the proposed risk model represents the probability of hazardous weather conditions that may affect the electricity grid operation at a given time. It is directly driven by the weather forecasts and is spatio-temporally correlated with various points in time and locations across the grid.

The *vulnerability* reflects the probability that a weather-driven hazardous condition will cause an event or undesirable state in the electricity grid. Such disorders may include the shortage in capacity and efficiency of the electricity generation by impacting the renewables, reliability of the grid equipment either through forced outages (faults) or stressful overloading conditions, electricity market violations, and unexpected load responses.

In the case where an undesirable condition in the grid is experienced in the face of a severe weather condition, the expected impact on the grid operation, in terms of economic loss, would be quantified as *consequence*. The consequences can be different depending on the user preference in various operation levels of the grid. The imposed outage cost, if the adverse weather condition leads to an electricity outage, or economic impact of operation adjustments in mitigation of grid violations can be quantified as the *economic consequence*. The total imposed costs corresponding to the failure of equipment i at time t , $C_k^t(E_i)$, is quantified in (23):

$$C_k^t(E_i) = C_{CM,i}^t + \sum_{d \in D} (C_{LR,i}^t + C_{CIC,i}^t) \quad (23)$$

The first monetary term in (23) is fixed and highlights the corrective maintenance cost to fix the damaged equipment. This cost, which in some cases can include the replacement cost of the equipment, also embraces the cost of labor, maintenance tools and materials. The second term (variable cost) includes the lost revenue cost imposed to the electric utility ($C_{LR,i}^t$) and the interruption costs imposed to the interrupted customers ($C_{CIC,i}^t$). The former cost function highlights the utility's lost revenue due to its inability to sell power during the replacement or corrective maintenance interval and can be quantified using (24) [45].

$$C_{LR,i}^t = \sum_{d \in D} (\lambda_d^t \cdot \text{EENS}_{d,i}^t) \quad (24)$$

where, λ_d^t is the electricity price (\$/MWh.) at load point d ; $\text{EENS}_{d,i}^t$ is the expected energy not supplied (MWh.) at load point d due to the failure of equipment i at time t . Here, the EENS index of reliability is calculated through the probabilistic analytical state enumeration method [45] by solving the following optimization problem (25) subject to a set of system constraints in (26):

$$\min_{i \in H} \sum_{d \in D} \left(\mathbf{IL}_{n,i}^t = P_{d_n}^t - P_{d_n,i}^{t, \text{supplied}} \right) \quad (25)$$

$$\begin{aligned} & \sum_{g \in I_{GU}^n} P_g^t - \sum_m V_n V_m (G_{nm} \cos \delta_{nm} + K_{nm} \sin \delta_{nm}) \\ & - P_d^n = 0, \quad \forall n \end{aligned} \quad (26.a)$$

$$\begin{aligned} & \sum_{g \in I_{GU}^n} Q_g^t - \sum_m V_n V_m (G_{nm} \sin \delta_{nm} - K_{nm} \cos \delta_{nm}) \\ & - Q_d^n = 0, \quad \forall n \end{aligned} \quad (26.b)$$

$$\begin{aligned} & P_{jnm} = V_n V_m (G_{nm} \cos \delta_{nm} + K_{nm} \sin \delta_{nm}) \\ & - G_{nm} V_n^2, \quad \forall j \end{aligned} \quad (26.c)$$

$$\begin{aligned} Q_{jnm} &= V_n V_m (G_{nm} \sin \delta_{nm} - K_{nm} \cos \delta_{nm}) \\ & + V_n^2 (K_{nm} - k_{nm}^{sh}), \quad \forall j \end{aligned} \quad (26.d)$$

$$P_{jnm}^2 + Q_{jnm}^2 \leq (S_j^{\max})^2, \quad \forall j \quad (26.e)$$

$$\delta_n^{\min} \leq \delta_n \leq \delta_n^{\max}, \quad \forall n \in N \quad (26.f)$$

$$V_n^{\min} \leq V_n \leq V_n^{\max}, \quad \forall n \in N \quad (26.g)$$

$$(P_g^t - r_g^{dn,t}) \xi_{g,i}^t \leq P_{g,i}^t \leq (P_g^t + r_g^{up,t}) \xi_{g,i}^t, \quad \forall g \in G \quad (26.h)$$

$$Q_g^{\min} \xi_{g,i}^t \leq Q_{g,i}^t \leq Q_g^{\max} \xi_{g,i}^t, \quad \forall g \in G \quad (26.i)$$

$$0 \leq r_g^t \leq \min(r_g^{\max}, \Delta_g), \quad \forall g \in G_R \quad (26.j)$$

$$0 \leq r_g^{dn,t} \leq \min(r_g^{dn,\max}, \Delta_g^{dn}), \quad \forall g \in I_{GU_R} \quad (26.k)$$

$$P_g^t + r_g^t \leq P_g^{\max}, \quad \forall g \in G_R \quad (26.l)$$

$$P_g^{\min} \leq P_g^t - r_g^{dn,t}, \quad \forall g \in I_{GU_R} \quad (26.m)$$

$$\sum_{g \in I_{GU,Z_m}} r_g^{up,t} \geq R_{Z_m}^{up,t}, \quad \forall m \quad (26.n)$$

$$\sum_{g \in I_{GU,Z_m}} r_g^{dn,t} \geq R_{Z_m}^{dn,t}, \quad \forall m \quad (26.o)$$

$$0 \leq \mathbf{IL}_{n,i}^t \leq P_{d_n}^t, \quad \forall n \in N, \forall i \in H \quad (26.p)$$

The optimization engine is formulated based on the Alternating Current (AC) power flow model for higher accuracy. Without loss of generality, the DC power flow model can also be approached if the computational requirements mandate [45]. Here, up to the third order of system contingencies are taken into account in the state enumeration technique utilized to evaluate the system reliability. At each contingency state, the optimization problem in (25) tries to minimize the total curtailed load during each contingency state i . As it can be seen in (25), the load outage at each load point is calculated by taking the difference of the actual demand and the supplied load following the contingency event. In order to reduce the simulation runtime, a risk-based contingency screening strategy is employed that first prioritizes the contingencies based on the product of their occurrence probability and consequence (i.e., the interrupted load) and then neglects the low-risk contingencies. Constraints (26.a), (26.b) represent two sets of N_b non-linear nodal active and reactive power balancing equations. Network constraints (26.c), (26.d) represent branch active and reactive power flow limits measured at bus n in direction towards bus m . The inequality constraints (26.e) consist of two sets of N_l apparent power flow limits corresponding to the ‘‘from’’ and ‘‘to’’ ends of each branch. Constraints (26.f), (26.g) reflect equality upper and lower limits on all bus voltage phase angles and magnitudes. Supply constraints are presented in (26.h), (26.i) that enforce the output of generating unit g to zero if it gets disconnected in the outage event i . If a generating unit g is available, the change of its active power output is limited to the predetermined margins. Outage of generating units in an outage event i is modeled through a vector of binary variables, $\xi_{g,i}^t$, with 1 denoting the availability of components and 0 otherwise. Constraints (26.j), (26.k) reflect

the reserve for each generating unit that must be positive and limited above by a reserve offer quantity as well as the physical ramp rate of the unit (Δg). Constraint (26.l), (26.m) enforce that the total amount of energy plus upward reserve of the generating unit does not exceed its capacity and the amount of energy minus downward reserve of the generating unit is limited to its minimum capacity. Constraints (26.n), (26.o) ensure that enough capacity is procured according to the reserve requirements in each region. Constraint (26.p) ensures that the interrupted load is less than the total demand at bus n .

Probability and duration of each contingency state i are calculated in (27) by employing the availability of online components (y) and unavailability of the failed ones (x) [45]; in particular, π_i is obtained in (27.a) by multiplying the availability of online components and unavailability of the failed ones in a contingency state i ; and τ_i^t is calculated in (27.b) using the failure rates of online components and repair rates of the failed ones in a given contingency state. Note that in all the above calculations, the common two-state Markov model for each system component is considered [45], [46].

$$\pi_i = \prod_{x \in \Omega_X} \frac{\nu_x}{(\gamma_x + \nu_x)} \times \prod_{y \in \Omega_Y} \frac{\gamma_y}{(\gamma_y + \nu_y)} \quad (27.a)$$

$$\tau_i^t = \left(\sum_{x \in X} \gamma_x + \sum_{y \in Y} \nu_y \right)^{-1}, \quad \forall i \in H \quad (27.b)$$

where, ν and γ are the failure rate and repair rate of equipment. The EENS index of reliability is calculated in (28):

$$\text{EENS}_{d,i}^t = \sum_{i \in H} \pi_i^t \cdot \tau_i^t \cdot \text{IL}_{d,i}^t, \quad \forall d \in D \quad (28)$$

The third variable term in the cost function (23) highlights the customer interruption costs due to an electricity outage event i at time t and is calculated through (29) [46]:

$$C_{\text{CIC},i}^t = \sum_{d \in D} \text{EENS}_{d,i}^t \cdot \text{VOLL}_d \quad (29)$$

where VOLL is the value of the lost load and represents the unit interruption cost for various customer sectors at a given load point. VOLL is directly correlated to the outage duration and is determined through historical data and customer surveys [46].

IV. WEATHER-DRIVEN MITIGATION STRATEGY: NETWORK TOPOLOGY CONTROL

As the grid keeps being exposed and vulnerability to weather-driven natural disasters (severe storms, hurricanes, etc.), research on enhancing the grid resilience in the face of such high impact low probability (HILP) events has been intensified over the past few years [47], [48]. Both “long-term” and “short-term” strategies for enhancing the grid resilience against the extreme conditions have been addressed in the literature [3]. The grid *structural resilience* is primarily focused toward deployment of the “grid hardening” plans through reinforcement, preventive maintenance of the critical assets, vegetation management, efficient allocation of flexible energy resources (e.g., storage units), etc. The *operational resilience* is targeted through fast

emergency response and remedial actions, defensive islanding, use of the micro-grids, etc. While the strategies above can be individually or collectively approached for enhancing the grid resilience, we are utilizing the network topology switching to mitigate the weather-driven risks across the grid.

The network topology control through transmission line switching offers the system operators a greater control in the flow of power. It is realized through harnessing the built-in flexibility of the network topology by temporarily removing lines from service [49]–[51]. By relying on the existing infrastructure and available generation resources with minimum additional costs, the proposed framework aims at safeguarding the grid by quickly and iteratively recovering from the consequences of weather-driven events (e.g., outages, congestions, grid violations, etc.) and realizing an enhanced grid operational resilience. The suggested framework is intended to be used as a predictive tool in operational planning timeframe.

A. Objective 1: Load Outage Recovery

If a hazardous weather event is forecasted as a result of which some load outages occur, the following optimization would be called in advance to mitigate the contingency.

$$\max \left(LS_{\dot{G} \cup \dot{K}} - \sum_{\forall n \in N} u_n \right) \quad (30)$$

Subject to:

$$\theta^{\min} \leq \theta_n - \theta_m \leq \theta^{\max}, \quad \forall k(m, n) \in K \quad (31.a)$$

$$\sum_{\forall k(n, \dots)} P_k - \sum_{\forall k(\dots, n)} P_k + \sum_{\forall g(n)} P_g = d_n - u_n \quad \forall n \in N \quad (31.b)$$

$$P_k^{\min}(1 - s_k) \leq P_k \leq P_k^{\max}(1 - s_k) \quad \forall k \in \hat{K} \quad (31.c)$$

$$B_k(\theta_n - \theta_m) - P_k + s_k \cdot M_k \geq 0 \quad \forall k \in \hat{K} \quad (31.d)$$

$$B_k(\theta_n - \theta_m) - P_k - s_k \cdot M_k \leq 0 \quad \forall k \in \hat{K} \quad (31.e)$$

$$P_k^{\min} \cdot s_k \leq P_k \leq P_k^{\max} \cdot s_k \quad \forall k \in \bar{K} \quad (31.f)$$

$$B_k(\theta_n - \theta_m) - P_k + (1 - s_k) \cdot M_k \geq 0 \quad \forall k \in \bar{K} \quad (31.g)$$

$$B_k(\theta_n - \theta_m) - P_k - (1 - s_k) \cdot M_k \leq 0 \quad \forall k \in \bar{K} \quad (31.h)$$

$$\max \{ P_g^{\min}, P_g^v - \tau r_g \} \leq P_g \leq \min \{ P_g^{\max}, P_g^v + \tau r_g \} \quad \forall g \in G \setminus \dot{G} \quad (31.i)$$

$$0 \leq u_n \leq d_n, \quad \forall n \in N \quad (31.j)$$

$$P_k = 0, \quad k \in \dot{K} \quad (31.k)$$

$$P_g = 0, \quad g \in \dot{G} \quad (31.l)$$

$$s_i = 0, \quad \forall i \in T \quad (31.m)$$

$$\sum_{\forall k \in K \setminus \dot{K}} s_k = 1 \quad (31.n)$$

$$s_k \in \{0, 1\}, \quad \forall k \in K \setminus \dot{K} \quad (31.o)$$

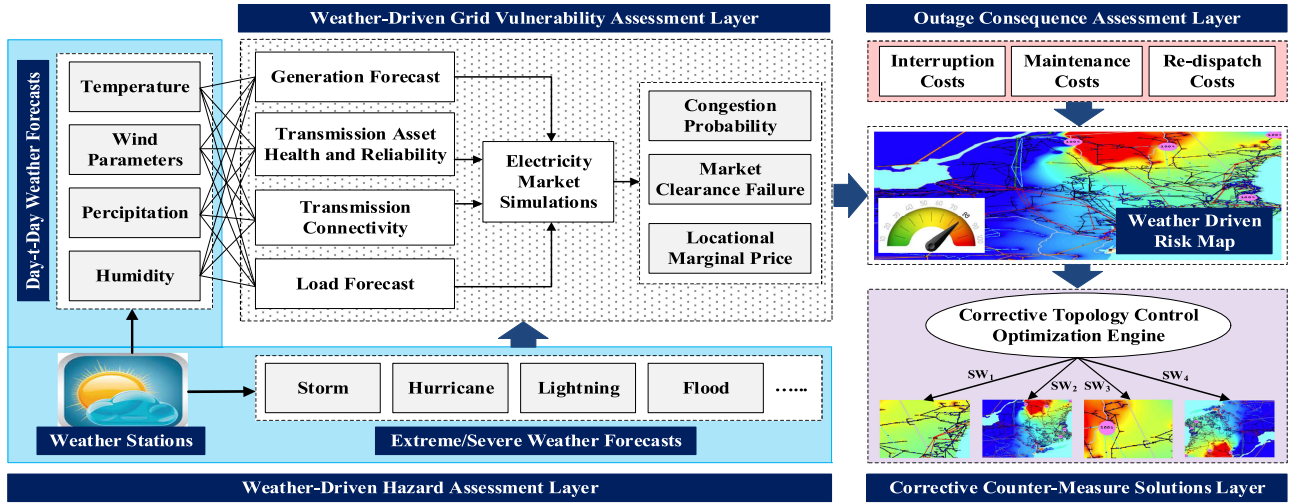


Fig. 5. The overall structure of the proposed framework for weather-resilient operation of the electricity grid.

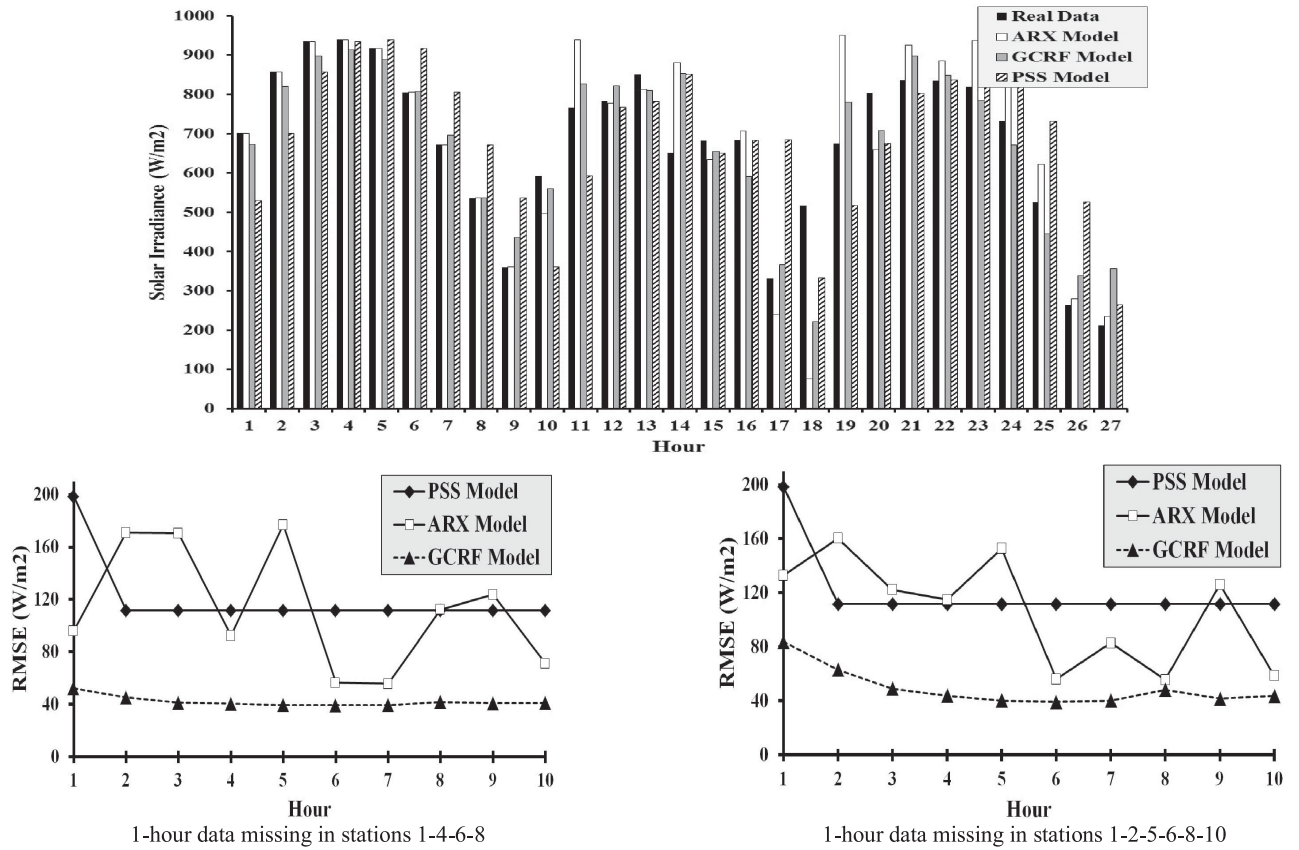


Fig. 6. Performance comparison of the suggested GCRF model with other known solar forecast techniques with and without missing data scenarios.

The above optimization model is a mixed integer linear programming problem based on the DCOPF formulation. The primary decision variables in the above optimization formulation are s_k and u_n , where s_k determines the switching action of line k (0: no switch; 1: switch) and u_n denotes the unfulfilled demand at bus n in case of a contingency. The objective (30) is to maximize the load outage recovery corresponding to the weather-driven contingency set $\dot{G} \cup \dot{K}$; The algorithm followed to solve the optimization model is the Binary Switching Tree

(BST) algorithm that iteratively finds the best line to switch and the optimal time-constrained generator re-dispatch until either the entire system demand is satisfied or a pre-specified stopping criterion is met. As a result, it provides multiple switching operations and corresponding re-dispatch actions to iteratively improve the load outage recovery. Additional details on the BST algorithm employed to solve this optimization problem can be found in [49]. Constraint (31.a) sets the angle difference range of the adjacent buses. The node balance constraints with

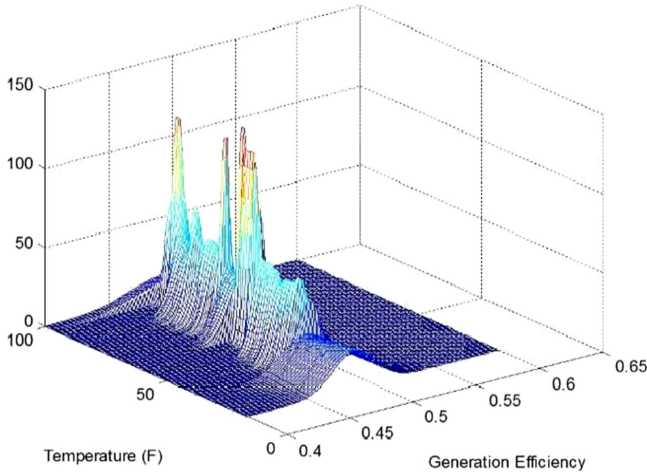


Fig. 7. Probability density function of thermal generation efficiency with the temperature input ranging from 17 °F to 100 °F.

modifications to account for partial demand fulfillment at each bus are presented in (31.b). Constraints (31.c) and (31.f) set the capacity limits of in service ($k \in \hat{K}$) and out of service ($k \in \bar{K}$) transmission lines, while constraints (31.d), (31.e), (31.g), and (31.h) determine the power flow through the lines. The re-dispatch constraints for the online generating units are characterized in (31.i), where P_g^v denotes the generator dispatch at node v . Constraints (31.j) set the bounds for unmet demand variable u_n at each bus. The line and generating unit outages are reflected in constraints (31.k) and (31.l), respectively. Constraints (31.m)–(31.o) are devised in addition to several other considerations, to be able to generate several topology control solutions per contingency (outage scenario) that would further improve the objective function, if subsequently implemented in a sequence. The benefit (the amount of Load Outage Recovery) obtained by the developed optimization model is attributed to both the switching actions and the 10-minute re-dispatch. Also, the topology control solutions should pass the AC feasibility and stability checks to be selected as the candidates for final implementation [49].

B. Objective 2: Congestion Relief

If price spikes are forecasted due to transmission congestions, the topology control scheme is called to relieve the transmission congestion, for which the objective is formulated in (32).

$$\max \sum_{\forall g \in G \setminus \hat{G}} c_g P_g \quad (32)$$

Without loss of generality, the constraints modeled earlier for load outage recovery are mostly valid for congestion-relief topology control scheme, with some minor changes. First, since there is no load outage, unmet demand variables u_n are no longer needed. Thus, u_n in constraint (31.b) and the entire constraint (31.j) should be removed. Second, instead of keeping track of the outage recovery percentage, one has to calculate and record the flow (or voltage) violations at each branch (or

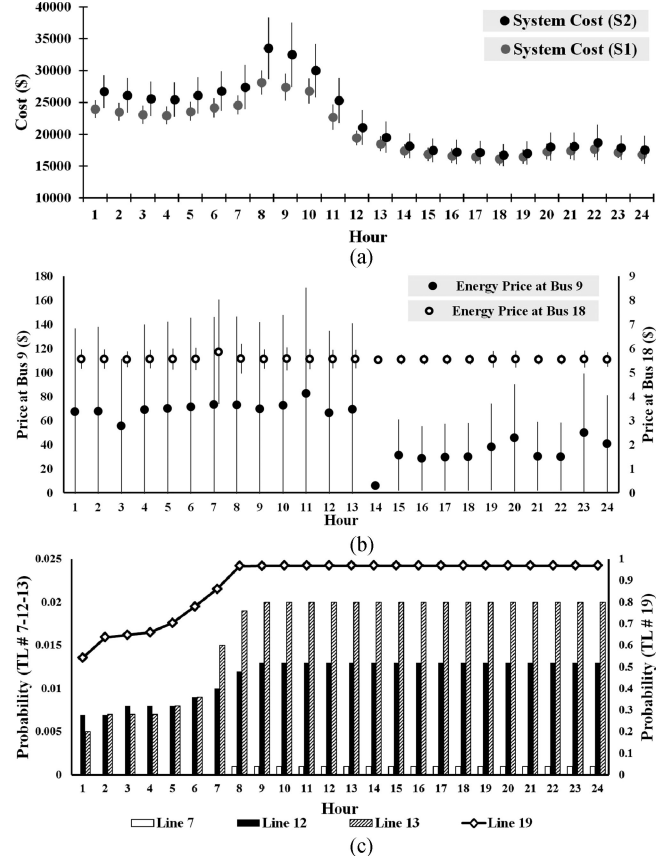


Fig. 8. Diurnal weather impacts on (a) system overall cost; (b) electricity market price; and (c) congestion probability of transmission lines.

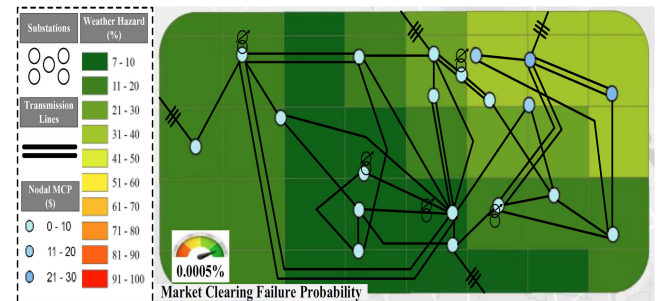


Fig. 9. Risk map generated for the studied system in face of normal weather conditions at hour 10.

node) corresponding to each new topology control solution generated.

The overall framework is generally demonstrated in Fig. 5. The proposed scheme leads to a more resilient electricity grid in the face of weather changes, prevents considerable financial and environmental losses, and reduces the risks to electric safety.

V. NUMERICAL CASE STUDIES

A modified section of the IEEE 73-bus test system is employed to investigate the applicability of the suggested framework, for which the one-line diagram is available in [52]. This transmission system contains 24 nodes, 17 load points, and 33 generating units connected by 38 transmission lines and 5

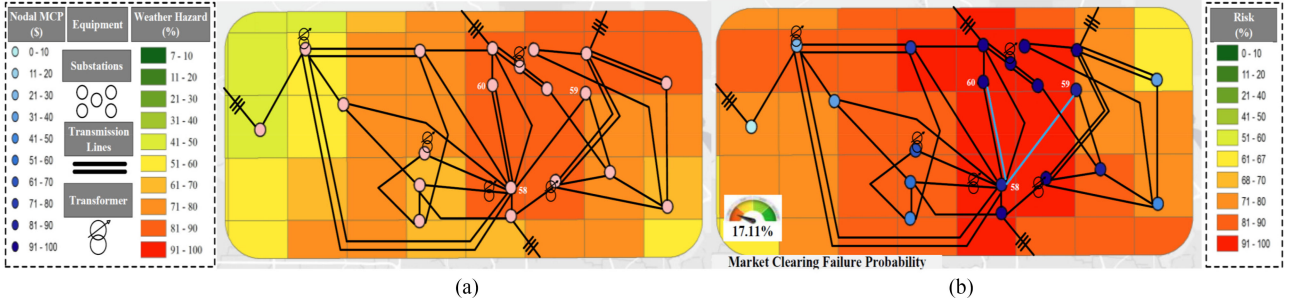


Fig. 10. (a) Hazard and (b) risk maps generated for the studied system in face of a severe weather condition at hour 10.

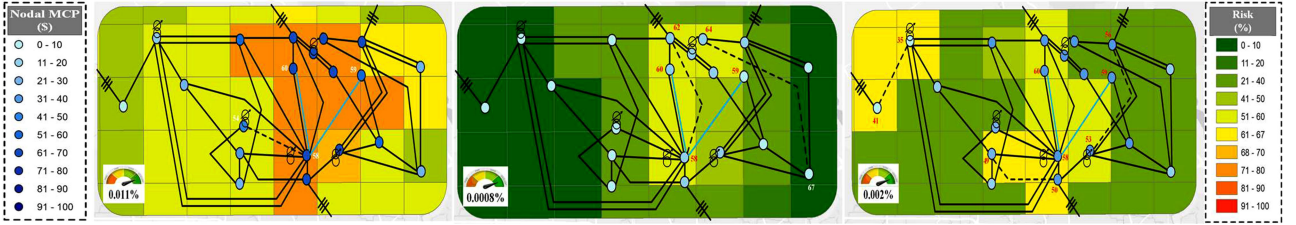


Fig. 11. Optimal topology control mitigation solutions (#1, #2, #3) and their impact on mitigating the imposed weather-driven risk at hour 10.

autotransformers at two voltage levels of 230 kV and 138 kV [51]. The loads are assumed to follow the pattern corresponding to the zone EKPC of the PJM system and all the employed data for various analyses are summarized in [52].

While the system power generation mostly comes from coal-fired thermal generating units, ten solar generating units are assumed to be located at buses 20 and 23 with the overall penetration rate equal to 5% of the total system generation capacity. The generated power through solar panels is forecasted in an hourly basis using the suggested GCRF model [(2)–(13)] for a 24 hour time interval. The performance of the proposed forecasting model is illustrated in Fig. 6 and is compared, in terms of root mean square error (RMSE), to other known techniques. As it can be realized from Fig. 6(a) and (b), the suggested weather-driven solar forecasting technique based on the GCRF model is more accurate than the other techniques even in cases of missing input data in several weather stations.

Regarding the coal-fired thermal generating units, Fig. 7 illustrates the result of probability density functions for the generation efficiency of the generating unit at bus 14, calculated through (1) based on the available historical data, when temperature is ranging from 17 °F to 100 °F, humidity is 90%, precipitation is 0 (inches), gauge height is 3.42 (m) and water discharge is 6990 (ft³/sec.).

A. Case Study 1: Normal Weather Projection

With the forecasted load and generation at each hour, the electricity market simulations are conducted. The system overall costs are illustrated in Fig. 8(a) where two scenarios, with (S2) and without (S1) considering the transmission equipment health indices and weather-driven line flow limits, are presented for the studied 24-hour period. The impact of weather variations on the energy price specifically on buses 9 and 18, as an example, is shown in Fig. 8(b) where the LMP at bus 9 is observed more

sensitive to weather variations over time; the weather-driven congestion probability of highly-vulnerable transmission lines are presented in Fig. 8(c). From Fig. 8, one can conclude that (1) the impact of weather variations on the electricity market is not only time-variant, but also space-variant; (2) some buses and transmission lines are particularly more sensitive to uncertainties imposed by weather. The risk map associated with projection of the forecasted weather hazard and calculated vulnerabilities is demonstrated in Fig. 9 for hour 10. The system operation risks in face of a normal weather condition at this hour are generally within the tolerable limits. Indicators for clearing prices at each load point and the electricity market clearance failure probability are also presented. The procedure above is repeated at each hour as the weather forecasts and system responses to such variations, and hence, the risk map varies hourly.

B. Case Study 2: Severe Weather Projection

In this case study, a severe weather regime at hour 10 is projected in the network. The weather-driven hazard map is illustrated in Fig. 10(a) where a part of the system is predicted to be exposed to a storm event. The developed risk-based analytical framework is simulated in this case, the system vulnerabilities in terms of electricity market failure probability, electricity prices at each load point, and the transmission line congestion probabilities are quantified, and the resulted risk map is illustrated in Fig. 10(b). It can be seen that as a result of this severe weather event, the congestion probabilities, and consequently the electricity prices at the mid-east part of the system, increase and two transmission lines (TL#92 connecting buses 58 to 59 and TL#93 connecting buses 58 to 60) would be out of service (denoted in blue) as a result of which 61.6 MW load outage occurs. The proposed corrective topology control optimization framework is simulated and three optimal

TABLE I
TOPOLOGY CONTROL MITIGATION SOLUTIONS IN RESPONSE TO THE
FORECASTED WEATHER CONTINGENCY: TL#92 AND TL#93 CONTINGENCY

#	Switching Line Solutions (#)	Load Shed Recovery (MW)	Percentage of Load Recovery (%)
1	86	20.8	33.6
2	105-95	61.6	100
3	72-77-99	36.2	58.7

topology change solutions (denoted in dashed lines) are suggested as mitigation actions (see Fig. 11). Additional details on switching solutions in response to the forecasted contingency are tabulated in Table I. The three optimal topology control solutions include a one-line (line 86 [bus54–bus58]) switching action as well as a two-line (line 105 [bus64–bus67] and line 95 [bus58–bus62]) and a three-line (line 72 [bus53–bus56], line 77 [bus49–bus50], and line 99 [bus35–bus41]) switching sequences all accompanied by a 10-min generation re-dispatch at each level. In case the solutions are composed of a sequence of switching actions, the sequence should be implemented in order to incrementally improve the load outage recovery and achieve the expected benefit eventually. With the changes that the optimal topology control solutions impose to the power flow and vulnerability indices, a considerable recovery of the outage in a timely manner can be realized leading to an improved system resilience in dealing with the aftermath of the HILP incidents. Note that the benefit (the amount of Load Outage Recovery) obtained by the developed optimization model is attributed to both the switching actions and the 10-minute re-dispatch. Specifically, if one were to perform only an optimal re-dispatch to recover as much interrupted load as possible (with no change in the network topology), the load outage recovery would be appreciably less. The updated risk maps accommodating each of the proposed mitigation solutions are demonstrated in Fig. 11, where it can be seen that different recovery plans migrate the system to a different operating condition with different levels of risk indicator. The system operator is provided with several recovery solutions and can make a final decision on which solution to implement eventually.

VI. CONCLUSION

In this paper, continuous weather-driven analytics for accurate spatial-temporal electricity generation forecasts were formulated and implemented for both renewable and conventional power generation based on the Gaussian Conditional Random Filed (GCRF) approach. It was numerically demonstrated that the proposed weather-driven forecasting method outperforms the traditional techniques. Employing the probabilistic load and generation forecasts, the electricity market simulation is conducted considering the weather-driven health and reliability status of transmission equipment over time. The spatial-temporal impact of weather variations on the energy price across the grid was quantified and comprehensively analyzed on a 24-bus part of the test system. The developed algorithms are integrated into a risk-based analytical framework where the electricity grid operation vulnerability can be quantified in face of the adverse high impact low probability (HILP) hazards from

meteorological predictions. A risk-based mitigation support tool based on corrective topology switching for load outage recovery was suggested where numerical results demonstrated that the proposed risk map and mitigation strategies could significantly help in fast and timely recovery of the weather-caused electricity outages by only harnessing the network built-in flexibility with minimum additional costs. The suggested decision support tool set enables the operators to predictively evaluate the high-risk weather hazards and consequently plan on how to safeguard the grid when exposed to such forecasted threats.

Future research may include application of advanced stochastic tools for the proposed modules and focuses on other risk mitigation strategies (e.g., micro grid and storage units).

REFERENCES

- [1] R. J. Campbell, "Weather-related power outages and electric system resiliency," Congressional Research Service, Library of Congress, 2012.
- [2] "Economic benefits of increasing electric grid resilience to weather outages," Executive Office of President Report, Aug. 2013.
- [3] "Enhancing the resilience of the nation's electricity systems," The National Academies Series (NAS) Consensus Study Report, Jul. 2017.
- [4] "A methodology for cost-risk analysis in the statistical validation of simulation models," National Climatic Data Center, 2012.
- [5] P. Dehghanian, S. Aslan, and P. Dehghanian, "Quantifying power system resiliency improvement using network reconfiguration," in *Proc. IEEE 60th Int. Midwest Symp. Circuits Syst.*, Boston, MA, USA, 2017, pp. 1364–1367.
- [6] E. D. Vugrin, D. E. Warren, and M. A. Ehlen, "A resilience assessment framework for infrastructure and economic systems: Quantitative and qualitative resilience analysis of petrochemical supply chains to a hurricane," *Process Safety Prog.*, vol. 30, no. 3, pp. 280–290, 2011.
- [7] C. Yang, A. Thatte, and L. Xie, "Multitime-scale data-driven spatio-temporal forecast of photovoltaic generation," *IEEE Trans. Sustain. Energy*, vol. 6, no. 1, pp. 104–112, Jan. 2015.
- [8] E. Lorenz, J. Hurka, D. Heinemann, and H. G. Beyer, "Irradiance forecasting for the power prediction of grid-connected photovoltaic systems," *IEEE J. Sel. Topics Appl. Earth Observ. Remote Sens.*, vol. 2, no. 1, pp. 2–10, Mar. 2009.
- [9] S. Lu *et al.*, "Machine learning based multi-physical-model blending for enhanced renewable energy forecast—Improvement via situation dependent error correction," in *Proc. Eur. Control Conf.*, Linz, Austria, Jul. 2015, pp. 283–290.
- [10] J. Dowell and P. Pinson, "Very-short-term probabilistic wind power forecasts by sparse vector auto-regression," *IEEE Trans. Smart Grid.*, vol. 7, no. 2, pp. 736–770, Mar. 2016.
- [11] R. Golombek, S. A. Kittelsen, and I. Haddeland, "Climate change: Impacts on electricity markets in Western Europe," *Climatic Change*, vol. 113, pp. 357–370, 2012.
- [12] B. Zhang, P. Dehghanian, and M. Kezunovic, "Simulation of weather impacts on the wholesale electricity market," in *Proc. 10th Int. Conf. Deregulated Electr. Market Issues South Eastern Europe*, Budapest, Hungary, 2015, pp. 1–7.
- [13] R. Handika, C. Truong, S. Trueck, and R. Weron, "Modelling price spikes in electricity markets—The impact of load, weather and capacity," Hugo Steinhaus Center, Wroclaw Univ. Sci. Technol., Wroclaw, Poland, HSC Res. Rep. HSC/14/08, Aug. 2014.
- [14] J. P. S. Catalão *et al.*, "Short-term electricity prices forecasting in a competitive market: A neural network approach," *Electr. Power Syst. Res.*, vol. 77, pp. 1297–1304, Aug. 2007.
- [15] S. Orme and J. Swansson, *Implications of Extreme Weather for the Australian National Electricity Market: Historical Analysis and 2019 Extreme Heatwave Scenario*. Sydney, NSW, Australia: Sapere Res. Group, 2014.
- [16] A. Godbole, "Climate change impacts on hydropower and the electricity market: A case study for Switzerland," master's thesis, Faculty Sci., Univ. Bern, Bern, Switzerland, 2014.
- [17] D. Rübhelke and S. Vögele, "Impacts of climate change on European critical infrastructures: The case of the power sector," *Environ. Sci. Policy*, vol. 14, pp. 53–63, Jan. 2011.
- [18] D. Zhang, W. Li, and X. Xiong, "Overhead line preventive maintenance strategy based on condition monitoring and system reliability assessment," *IEEE Trans. Power Syst.*, vol. 29, no. 4, pp. 1839–1846, Apr. 2014.

- [19] M. Bockarjova and G. Anderson, "Transmission line conductor temperature impact on state estimation accuracy," in *Proc. IEEE Power Tech. Conf.*, Lausanne, Switzerland, 2007, pp. 701–706.
- [20] D. Fay and J. V. Ringwood, "On the influence of weather forecast errors in short-term load forecasting models," *IEEE Trans. Power Syst.*, vol. 25, no. 3, pp. 1751–1758, Aug. 2010.
- [21] A. P. Douglas, A. M. Breipohl, F. N. Lee, and R. Adapa, "The impacts of temperature forecast uncertainty on Bayesian load forecasting," *IEEE Trans. Power Syst.*, vol. 13, no. 4, pp. 1507–1513, 1998.
- [22] K. Methaprayoon *et al.*, "Multistage artificial neural network short-term load forecasting engine with front-end weather forecast," in *Proc. IEEE Ind. Commercial Power Syst. Tech. Conf.*, Apr. 2006, pp. 1–7.
- [23] M. Yeary *et al.*, "A brief overview of weather radar technologies and instrumentation," *IEEE Instrum. Meas. Mag.*, vol. 17, no. 5, pp. 10–15, Oct. 2014.
- [24] J. Wang, X. Xiong, Z. Li, W. Wang, and J. Zhu, "Wind forecast-based probabilistic early warning method of wind swing discharge for OHTLs," *IEEE Trans. Power Del.*, vol. 31, no. 5, pp. 2169–2178, Oct. 2016.
- [25] Y. Xie *et al.*, "Space-time early warning of power grid fault probability by lightning," *Autom. Electr. Power Syst.*, vol. 37, no. 17, pp. 44–51, 2013.
- [26] P. Dehghanian, "Quantifying power system resilience improvement through network reconfiguration in cases of extreme emergencies," M.Sc. thesis, Dept. Eng. Technol., Texas State Univ., San Marcos, TX, USA, 2017.
- [27] S. C. Nierop, "Envisioning resilient electrical infrastructure: A policy framework for incorporating future climate change into electricity sector planning," *Environ. Sci. Policy*, vol. 40 pp. 78–84, Apr. 2014.
- [28] M. Panteli and P. Mancarella, "Modeling and evaluating the resilience of critical electrical power infrastructure to extreme weather events," *IEEE Syst. J.*, vol. 11, no. 3, pp. 1733–1742, Sep. 2017.
- [29] N. Amjadya, F. Keyniaa, and H. Zareipour, "Short-term wind power forecasting using ridgelet neural network," *Electr. Power Syst. Res.*, vol. 81, pp. 2099–2107, 2011.
- [30] L. A. Fernandez-Jimenez *et al.*, "Short-term power forecasting system for photovoltaic plants," *Renew. Energy*, vol. 44, pp. 311–317, 2012.
- [31] D. L. McLeish, "A robust alternative to the normal distribution," *Can. J. Statist.*, vol. 10, no. 2, pp. 89–102, Jun. 1982.
- [32] N. Y. Yirusen and J. Melero, "Probability density function selection based on the characteristics of wind speed data," *J. Phys.*, vol. 753, 2016, Art. no. 032067.
- [33] E. K. Akpinar and S. Akpinar, "A statistical analysis of wind speed data used in installation of wind energy conversion systems," *Energy Convers. Manage.*, vol. 4, no. 46, pp. 515–532, 2005.
- [34] E. C. Morgan, M. Lackner, R. M. Vogel, and L. G. Baise, "Probability distributions for offshore wind speeds," *Energy Convers. Manage.*, vol. 52, pp. 15–26, 2011.
- [35] H. Fischer, *A History of the Central Limit Theorem from Classical to Modern Probability Theory*. New York, NY, USA: Springer, 2010.
- [36] V. Radosavljevic, S. Vucetic, and Z. Obradovic, "Neural Gaussian conditional random fields," in *Machine Learning and Knowledge Discovery in Databases*. Berlin, Germany: Springer, 2014, pp. 614–629.
- [37] V. Radosavljevic, "Gaussian conditional random fields for regression in remote sensing," Ph.D. dissertation, Dept. Comput. Inf. Sci., Temple Univ., Philadelphia, PA, USA, 2012.
- [38] R. Vilaithong, S. Tenbohlen, and T. Stirl, "Neural network for transformer top-oil temperature prediction," in *Proc. XVth Int. Symp. High Voltage Eng.*, Ljubljana, Slovenia, Aug. 2007, pp. 1–6.
- [39] A. E. B. Abu-Elanien, M. M. A. Salama, and M. Ibrahim, "Determination of transformer health condition using artificial neural networks," in *Proc. Int. Symp. Innovations Intell. Syst. Appl.*, Istanbul, Turkey, 2011, pp. 1–5.
- [40] T. Dokic *et al.*, "Risk assessment of a transmission line insulation breakdown due to lightning and severe weather," in *Proc. 49th Hawaii Int. Conf. Syst. Sci.*, Big Island, HI, USA, Jan. 2016, pp. 2488–2497.
- [41] Y. Q. Ding *et al.*, "The effect of calculated wind speed on the capacity of dynamic line rating," in *Proc. IEEE Int. Conf. High Voltage Eng. Appl.*, Chengdu, China, 2016, pp. 1–5.
- [42] M. Bartos *et al.*, "Impacts of rising air temperatures on electric transmission ampacity and peak electricity load in the United States," *Environ. Res. Lett.*, vol. 11, Nov. 2016, Art. no. 114008.
- [43] O. H. Abdalla *et al.*, "Weather-based ampacity of overhead transmission lines," in *Proc. 4th Gen. Conf. Arab Union Elect. Exhib.*, 2013, pp. 1–7.
- [44] J. F. Hall and A. K. Deb, "Prediction of overhead transmission line ampacity by stochastic and deterministic models," *IEEE Trans. Power Del.*, vol. 3, no. 2, pp. 789–800, Apr. 1988.
- [45] R. Billinton and R. N. Allan, *Reliability Evaluation of Engineering Systems: Concepts and Techniques*, 2nd ed. New York, NY, USA: Plenum, 1992.
- [46] W. Li, *Probabilistic Transmission System Planning*. Hoboken, NJ, USA: Wiley, 2011.
- [47] M. Panteli *et al.*, "Power systems resilience assessment: Hardening and smart operational enhancement strategies," *Proc. IEEE*, vol. 105, no. 7, pp. 1202–1213, Jul. 2017.
- [48] B. Zhang, P. Dehghanian, and M. Kezunovic, "Optimal allocation of PV generation and battery storage for enhanced resilience," *IEEE Trans. Smart Grid*, to be published, doi: 10.1109/TSG.2017.2747136.
- [49] P. Dehghanian *et al.*, "Flexible implementation of power system corrective topology control," *Electr. Power Syst. Res.*, vol. 128, pp. 79–89, Nov. 2015.
- [50] P. Dehghanian, S. Aslan, and P. Dehghanian, "Maintaining electric system safety through an enhanced network resilience," *IEEE Trans. Ind. Appl.*, vol. 54, no. 5, pp. 4927–4937, Sep./Oct. 2018.
- [51] P. Dehghanian and M. Kezunovic, "Probabilistic decision making for the bulk power system optimal topology control," *IEEE Trans. Smart Grid*, vol. 7, no. 4, pp. 87–97, Jun. 2016.
- [52] IEEE RTS Task Force of APM Subcommittee, "IEEE reliability test system," *IEEE Trans. Power Appl. Syst.*, vol. PAS-98, no. 6, pp. 2047–2054, Nov. 1979.
- [53] 2018. [Online]. Available: <https://dehghanian.net/wp-content/uploads/2017/12/IEEE-TSTE-Data.pdf>

Payman Dehghanian (S'11–M'17) received the B.Sc. degree from the University of Tehran, Tehran, Iran, in 2009, the M.Sc. degree from the Sharif University of Technology, Tehran, in 2011, and the Ph.D. degree from Texas A&M University, College Station, TX, USA, in 2017, all in electrical engineering. He is an Assistant Professor with the Department of Electrical and Computer Engineering, George Washington University, Washington, DC, USA. His research interests include power system protection and control, power system reliability and resiliency, asset management, and smart electricity grid applications.

Dr. Dehghanian is the recipient of the 2013 IEEE Iran Section Best M.Sc. Thesis Award in Electrical Engineering, the 2014 and 2015 IEEE Region 5 Outstanding Professional Achievement Awards, and the 2015 IEEE-HKN Outstanding Young Professional Award.

Bei Zhang (M'17) received the B.S. and M.S. degrees from Shanghai Jiao Tong University, Shanghai, China, in 2009 and 2012, respectively, and the Ph.D. degree in electrical engineering from Texas A&M University, College Station, TX, USA, in 2017. She is currently with GE Power, Schenectady, NY, USA. Her research interests include power system reliability, electric vehicles, and electricity market.

Tatjana Dokic (S'10) received the B.Sc. and M.Sc. degrees in electrical and computer engineering from the University of Novi Sad, Novi Sad, Serbia, in 2012. She is a graduate student with Texas A&M University, College Station, TX, USA. Her main research interests include power system asset and outage management, weather impacts on power systems, big data for power system applications, vegetation management, insulation coordination, and fault location.

Mladen Kezunovic (S'77–M'80–SM'85–F'99–LF'17) received the Dipl. Ing., M.S., and Ph.D. degrees in electrical engineering in 1974, 1977, and 1980, respectively. He has been with Texas A&M University, College Station, TX, USA, for 31 years, where he is currently a Regents Professor and an Eugene E. Webb Professor, the Director of the Smart Grid Center, and the Site Director of "Power Engineering Research Center, PSec" consortium. He is currently the Principal of XpertPower Associates, a consulting firm specializing in power systems data analytics. His expertise is in protective relaying, automated power system disturbance analysis, computational intelligence, data analytics, and smart grids. He has authored more than 550 papers, given more than 120 seminars, invited lectures and short courses, and consulted for more than 50 companies worldwide.

Dr. Kezunovic is a Fellow of CIGRE and a registered Professional Engineer in Texas.